Supplementary Information for "Higgs transition from a magnetic Coulomb liquid to a ferromagnet in $Yb_2Ti_2O_7$"

Lieh-Jeng Chang[1,2], Shigeki Onoda[3], Yixi Su[4], Ying-Jer Kao[5], Ku-Ding Tsuei[6], Yukio Yasui[7,8], Kazuhisa Kakurai[2] & Martin Richard Lees[8].

[1] *Department of Physics, National Cheng Kung University, Tainan 70101, Taiwan,*
[2] *Quantum Beam Science Directorate, Japan Atomic Energy Agency, Tokai, Ibaraki 319-1195, Japan,*
[3] *Condensed Matter Theory Laboratory, RIKEN, Wako, Saitama 351-0198, Japan,*
[4] *Jülich Centre for Neutron Science JCNS-FRM II, Forschungszentrum Jülich GmbH, Outstation at FRM II, Lichtenbergstrasse 1, D-85747 Garching, Germany,*
[5] *Department of Physics and Center for Advanced Study in Theoretical Science, National Taiwan University, Taipei 10607, Taiwan,*
[6] *National Synchrotron Radiation Research Center, Hsinchu 30076, Taiwan,*
[7] *Department of Physics, Division of Material Science, Nagoya University, Furo-cho, Chikusa-ku, Nagoya 464-8602, Japan ,*
[8] *Department of Physics, Meiji University, Kawasaki 214-8571, Japan and*
[9] *Department of Physics, University of Warwick, Coventry CV4 7AL, United Kingdom.*

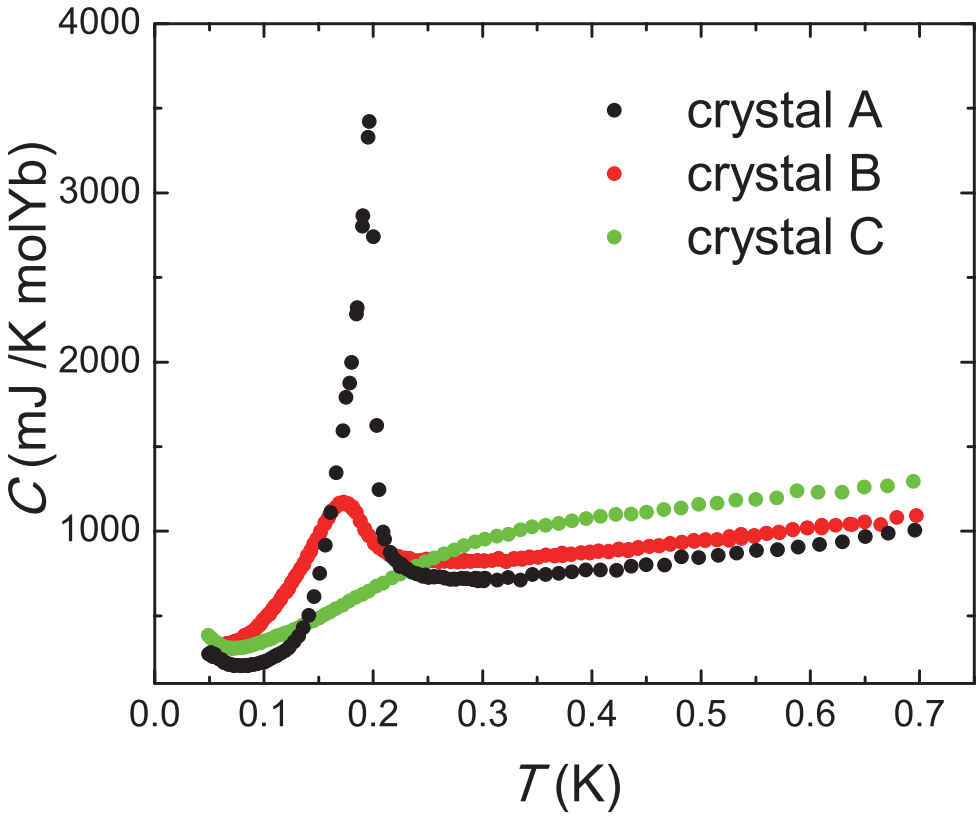

Supplementary Figure S1: **Low-temperature specific heat versus temperature for three single crystals of $Yb_2Ti_2O_7$.** Sample A was used for the polarized neutron-scattering experiments reported in the main text. The heat capacity measurements were carried out in a Quantum Design Physical Property Measurement System (PPMS) using a pulse-relaxation calorimetry technique.

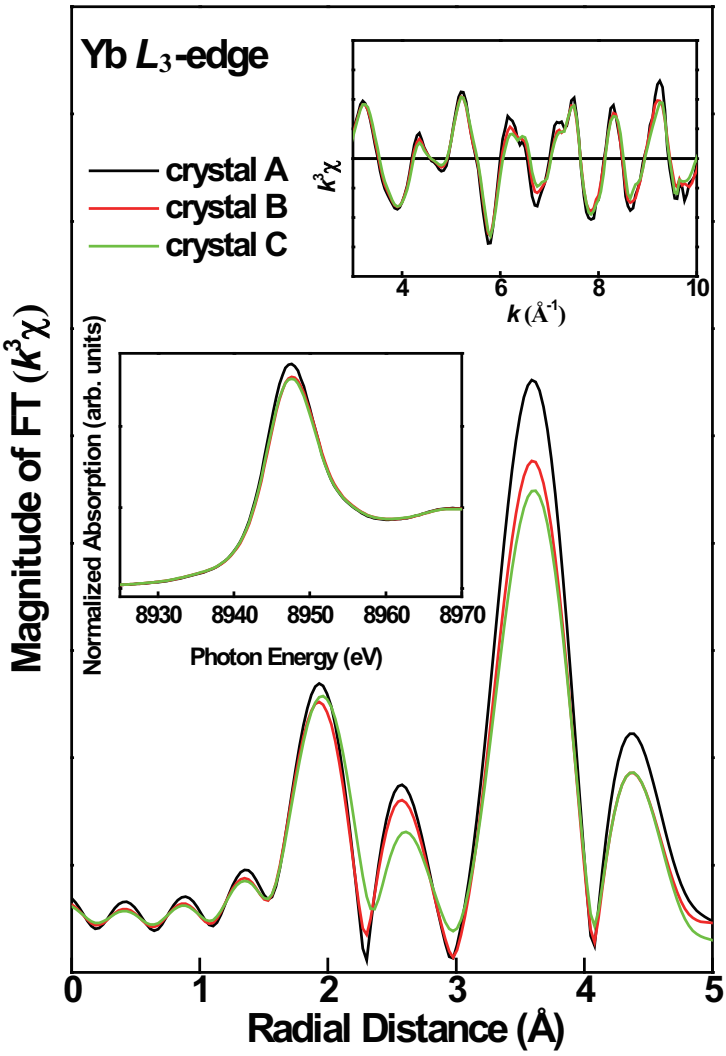

Supplementary Figure S2: **EXAFS radial distribution functions at the Yb L_3-edge.** The curves were obtained from the Fourier transform of raw spectra in the upper inset. The near edge x-ray absorption spectra (XAS), shown in the middle inset, reveal only the Yb^{3+} peak at 8947 eV. The data are presented for crystals A (black), B (red) and C (green).

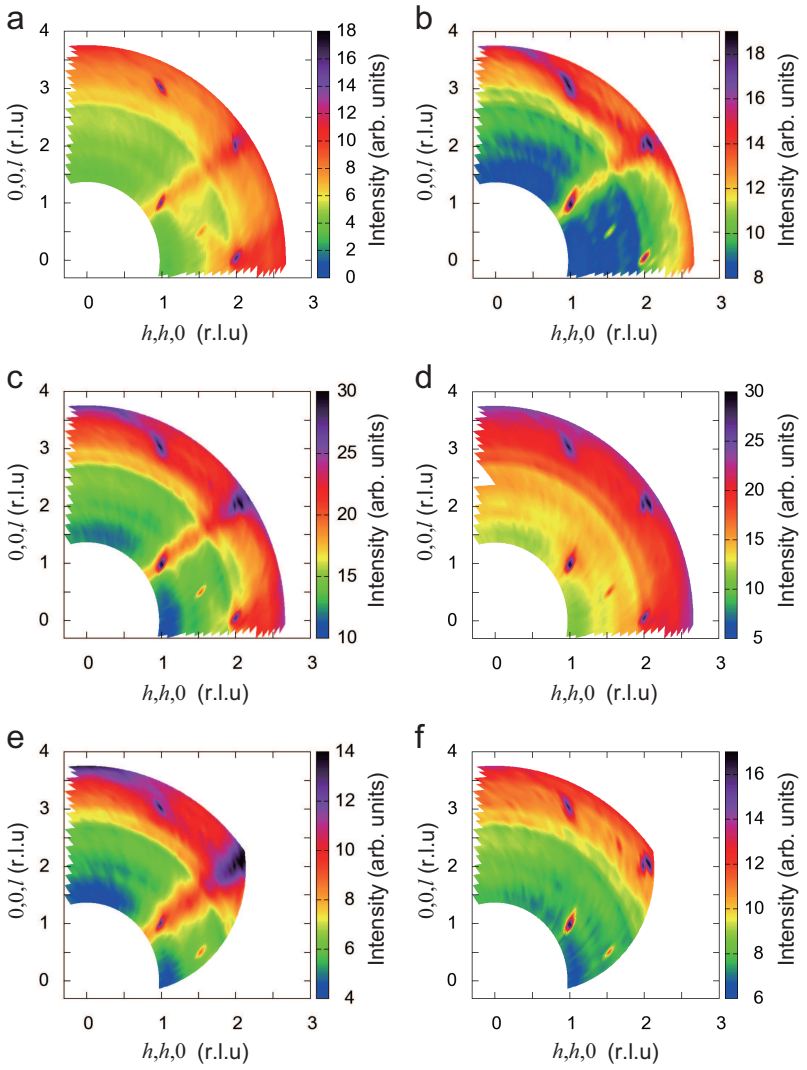

Supplementary Figure S3: **Raw polarized neutron-scattering cross-sections.** The data were taken in the energy-integrated diffraction mode at DNS. (**a**,**b**,**c**) The SF, NSF, and total cross-sections, respectively, in the Z-direction polarized neutron-scattering measurements at $T = 0.3$ K. (**d**) The total cross-section in the Z-direction polarized neutron-scattering measurements at $T_0 = 0.04$ K. (**e**,**f**) The SF and NSF cross-sections, respectively, in the X-direction polarized neutron-scattering measurements at $T_X = 0.7$ K. Sharp peaks at reciprocal lattice vectors (111), (002), (220) and so on are dominated by the nuclear contributions. The weak peaks at $(1.5, 1.5, 0.5)$ and (112) are attributed to contamination from higher order scattering and are not intrinsic.

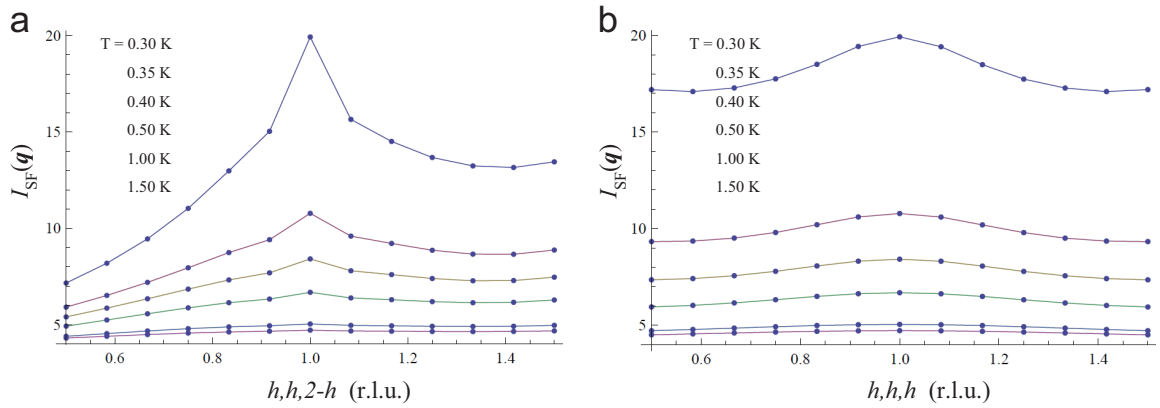

Supplementary Figure S4: **Temperature dependence of the theoretically calculated Z-polarized neutron-scattering cross-section in the SF channel.** (**a**) The intensity along the $[11-1]$ cut through the (111) point. (**b**) The intensity along the $[111]$ cut through the (111) point.

Supplementary Methods

Background subtraction

Here, we explain how we derive the Z-direction polarized diffuse magnetic scattering profiles at 0.3 K shown in Fig. 2a of the main text from the raw data shown in Supplementary Fig. S3. We estimate and subtract the background levels for the SF and NSF channels as follows.

Because of the formation of a long-range ferromagnetic order and the loss of the $[111]$-rod diffuse scattering intensity well below $T_{\rm C}$ K, the sum of the SF and NSF channels at $T_0 = 0.04$ K can be roughly regarded as a temperature-independent background due to the nuclear coherent and incoherent scattering cross-sections;

$$\left(\frac{d\sigma}{d\Omega}\right)^{\rm Total\ bg} = N^*N + I_{SI} \approx \left(\frac{d\sigma}{d\Omega}\right)^{\rm Total}_{T_0}, \tag{S1}$$

except around the Bragg peak positions where we suffer from a slight overestimate due to the magnetic Bragg-peak intensities. On the other hand, the SF and NSF cross-section profiles obtained at 0.04 K cannot be used as background levels, because the incident neutron spins are fully depolarized at 0.04 K, while they are only partially depolarized at 0.3 K, as is clear from Fig. 3e of the main text.

Note that the spin flipping ratio is defined as the ratio of the NSF to SF scattering intensity at a Bragg-peak position (111), where nuclear coherent scattering cross-section N^*N, which appears only in the NSF channel according to Eqs. (5) and (6) as well as Eqs. (3) and (4), dominates over the other contributions. Then, it is reasonable to assume that the SF and NSF cross-sections observed at a temperature T with the Z- and X-direction polarized neutron-scattering measurements take the forms

$$\left(\frac{d\sigma}{d\Omega}\right)^{Z-{\rm SF}}_{T} \approx \frac{(M^*_{\perp Y}M_{\perp Y})_T + \frac{2}{3}I_{SI} + r_T^{-1}\left[(M^*_{\perp Z}M_{\perp Z})_T + N^*N + \frac{1}{3}I_{SI}\right]}{1 + r_T^{-1}}, \tag{S2}$$

$$\left(\frac{d\sigma}{d\Omega}\right)^{Z-{\rm NSF}}_{T} \approx \frac{r_T^{-1}\left[(M^*_{\perp Y}M_{\perp Y})_T + \frac{2}{3}I_{SI}\right] + (M^*_{\perp Z}M_{\perp Z})_T + N^*N + \frac{1}{3}I_{SI}}{1 + r_T^{-1}}, \tag{S3}$$

$$\left(\frac{d\sigma}{d\Omega}\right)^{X-{\rm SF}}_{T} \approx \frac{(M^*_{\perp Y}M_{\perp Y} + M^*_{\perp Z}M_{\perp Z})_T + \frac{2}{3}I_{SI} + r_T^{-1}\left[N^*N + \frac{1}{3}I_{SI}\right]}{1 + r_T^{-1}}, \tag{S4}$$

$$\left(\frac{d\sigma}{d\Omega}\right)^{X-{\rm NSF}}_{T} \approx \frac{r_T^{-1}\left[(M^*_{\perp Y}M_{\perp Y} + M^*_{\perp Z}M_{\perp Z})_T + \frac{2}{3}I_{SI}\right] + N^*N + \frac{1}{3}I_{SI}}{1 + r_T^{-1}}. \tag{S5}$$

Using Eqs. (S4) and (S5), the magnetic cross-section can be eliminated and the temperature-independent purely X-NSF background cross-section is given by

$$N^*N + \frac{1}{3}I_{SI} = \frac{\left(\frac{d\sigma}{d\Omega}\right)^{X-{\rm NSF}}_{T_X} - r_{T_X}^{-1}\left(\frac{d\sigma}{d\Omega}\right)^{X-{\rm SF}}_{T_X}}{1 - r_{T_X}^{-1}}, \tag{S6}$$

at a temperature T_X. For a higher accuracy, it is better to take the data with a larger spin flipping ratio r_{T_X}, and thus we take $T_X = 0.7$ K where $r_{T_X} \sim 14.97$ (Fig. 3e of the main text). The raw data for the X-direction polarized elastic diffuse neutron-scattering experiments are shown in Supplementary Figs. S3 e,f. In fact, the $\boldsymbol{Q}$-space region where the X-direction polarized experiments have been performed does not cover all the reciprocal space required for this analysis. Nevertheless, the profile for Eq. (S6) obtained from Supplementary Figs. S3 e,f at $T_X = 0.7$ K is reproduced to an accuracy of 10%, except at the Bragg-peak positions, by multiplying the profile for $\left(\frac{d\sigma}{d\Omega}\right)^{\rm total}_{T_0}$ at $T_0 = 0.04$ K shown in Supplementary Fig. S3d by an overall scale factor 0.6. This allows us to simulate the NSF background profile for Eq. (S6) in the whole required area of the (hhl) plane.

Now, we can express the background cross-sections for the SF and NSF channels in the Z-direction polarized neutron-scattering experiments as

$$\left(\frac{d\sigma}{d\Omega}\right)^{Z-\rm SF\ bg}_{T} = \frac{[N^*N + I_{SI}] - (1 - r_T^{-1})\left[N^*N + \frac{1}{3}I_{SI}\right]}{1 + r_T^{-1}}, \tag{S7}$$

$$\left(\frac{d\sigma}{d\Omega}\right)^{Z-\rm NSF\ bg}_{T} = \frac{r_T^{-1}\left[N^*N + I_{SI}\right] + (1 - r_T^{-1})\left[N^*N + \frac{1}{3}I_{SI}\right]}{1 + r_T^{-1}}, \tag{S8}$$

where $[N^*N + I_{SI}]$ and $\left[N^*N + \frac{1}{3}I_{SI}\right]$ are given by Eqs. (S1) and (S6), respectively. The spin flipping ratio at $T = 0.3$ K is given by $r_T = 8.7$ (Fig. 3e of the main text).

In principle, we should also be able to eliminate a small (11.5%) mixing of $M^*_{\perp Z}M_{\perp Z}$ in the SF channel and of $M^*_{\perp Y}M_{\perp Y}$ in the NSF channel at 0.3 K. However, this effect is found to be small compared with the accuracy of the background subtraction.

Mean-field theory and random phase approximations

The classical mean-field (MF) Hamiltonian is given by

$$H_{MF} = \frac{1}{2}\sum_{\boldsymbol{Q}}\sum_{\mu,\nu=x,y,z}\sum_{i,j=0}^{3}\langle 2S^{\mu}_{-\boldsymbol{Q},i}\rangle h^{\mu\nu}_{\boldsymbol{Q},i,j}\langle 2S^{\mu}_{\boldsymbol{Q},j}\rangle \tag{S9}$$

where $h^{\mu\nu}_{\boldsymbol{Q},i,j}$ is obtained from the Fourier transform of the full Hamiltonian $(H_D + H_{se})$ given in the main text[16,19], and i and j denote indices for the Yb sites at $\boldsymbol{R} + \boldsymbol{a}_i$ $(i = 0, \cdots, 3)$ with fcc lattice vectors $\boldsymbol{R}$ and $\boldsymbol{a}_0 = (0,0,0)$, $\boldsymbol{a}_1 = a(0, \frac{1}{4}, \frac{1}{4})$, $\boldsymbol{a}_2 = a(\frac{1}{4}, 0, \frac{1}{4})$, and $\boldsymbol{a}_3 = a(\frac{1}{4}, \frac{1}{4}, 0)$, and the cubic lattice constant a. The local coordinate frames are taken as

$$\boldsymbol{e}^x_0 = -\frac{1}{\sqrt{6}}(1,1,-2), \quad \boldsymbol{e}^y_0 = -\frac{1}{\sqrt{2}}(-1,1,0), \quad \boldsymbol{e}^z_0 = \frac{1}{\sqrt{3}}(1,1,1), \tag{S10}$$

$$\boldsymbol{e}^x_1 = -\frac{1}{\sqrt{6}}(1,-1,2), \quad \boldsymbol{e}^y_1 = -\frac{1}{\sqrt{2}}(-1,-1,0), \quad \boldsymbol{e}^z_1 = \frac{1}{\sqrt{3}}(1,-1,-1), \tag{S11}$$

$$\boldsymbol{e}_2^x = -\frac{1}{\sqrt{6}}(-1,1,2)\,, \quad \boldsymbol{e}_2^y = -\frac{1}{\sqrt{2}}(1,1,0)\,, \quad \boldsymbol{e}_2^z = \frac{1}{\sqrt{3}}(-1,1,-1), \tag{S12}$$

$$\boldsymbol{e}_3^x = -\frac{1}{\sqrt{6}}(-1,-1,-2)\,, \quad \boldsymbol{e}_3^y = -\frac{1}{\sqrt{2}}(1,-1,0)\,, \quad \boldsymbol{e}_3^z = \frac{1}{\sqrt{3}}(-1,-1,1), \tag{S13}$$

to maximally exploit the symmetry of the system. In particular, the z axis points to the $\langle 111\rangle$ direction of the Ising magnetic moment. This in turn introduces the following simple bond-dependent phases $\phi_{\boldsymbol{r},\boldsymbol{r}'} = \phi_{ij} = \phi_{ji}$ in the two superexchange terms proportional to q and K which break the planar U(1) pseudospin symmetry;

$$\phi_{01} = \phi_{23} = -\frac{2\pi}{3}, \;\; \phi_{02} = \phi_{31} = \frac{2\pi}{3}, \;\; \phi_{03} = \phi_{12} = 0, \tag{S14}$$

where (i,j) is a pair of sublattice indices for $\boldsymbol{r}$ and $\boldsymbol{r}'$.

The Ewald summation technique was employed to calculate the long-range magnetic dipolar interaction. Then, the eigenvalue problem is solved for each $\boldsymbol{Q}$ as

$$\sum_{\nu} h^{\mu\nu}_{\boldsymbol{Q},i,j}\phi^{\nu}_{\boldsymbol{Q},n,j} = \varepsilon_{\boldsymbol{Q},n}\phi^{\mu}_{\boldsymbol{Q},n,i}, \tag{S15}$$

where n labels the twelve eigenvalues/eigenstates. The magnetic neutron-scattering cross-sections at a temperature T are then calculated with the random phase approximation (RPA)[34,44] as

$$I(\boldsymbol{Q}) = \sum_{n}\sum_{i,j=1}^{4} f^{\mu\nu}_{\boldsymbol{Q},i,j}\frac{\phi^{\mu}_{-\boldsymbol{Q},n,i}\phi^{\nu}_{\boldsymbol{Q},n,j}}{3+\epsilon_{\boldsymbol{Q},n}/T}. \tag{S16}$$

where

$$f^{\mu\nu}_{\boldsymbol{Q},i,j} = \frac{1}{4|\boldsymbol{Q}|^4}\left[\boldsymbol{Z}\cdot(\boldsymbol{Q}\times(g_\mu\boldsymbol{e}_i^\mu\times\boldsymbol{Q}))\right]\left[\boldsymbol{Z}\cdot(\boldsymbol{Q}\times(g_\nu\boldsymbol{e}_j^\nu\times\boldsymbol{Q}))\right], \tag{S17}$$

with $\boldsymbol{Z} = (1,-1,0)/\sqrt{2}$ for the NSF channel and

$$f^{\mu\nu}_{\boldsymbol{Q},i,j} = \frac{1}{4|\boldsymbol{Q}|^4}\left[\boldsymbol{Q}\times(g_\mu\boldsymbol{e}_i^\mu\times\boldsymbol{Q})\right]\cdot\left[\boldsymbol{Q}\times(g_\nu\boldsymbol{e}_j^\nu\times\boldsymbol{Q})\right] \tag{S18}$$

for the total. The SF channel is obtained as the difference between the above two.

In our case of $J > 0$, while $\delta > 0$ leads to profiles analogous to the nearest-neighbour Ising exchange or dipolar spin ice[10], a choice of $\delta < 0$ produces various profiles depending on the other relative coupling constants q and K. The best fit to our experimentally obtained and analysed magnetic scattering profiles at 0.3 K, shown in Fig. 2a of the main text, was obtained with $(J,\delta,q,K) = (0.68\text{ K}, -0.8, 0.2, -1.0)$, as shown in Fig. 2b of the main text. This set of parameter values is compared to the result from the spin-wave fitting[20], which is translated into $J = 2.0\pm0.5$ K, $\delta = -0.6\pm0.3$, $q = 0.6\pm0.3$ and $K = -1.6\pm\sim0.4$ in the present notation. Our exchange energy scale is smaller by a factor of 2-3. The discrepancy in J may be partly

attributed to an overestimate of the temperature at which an RPA instability occurs, ~ 0.29 K. This gives $\theta_{\rm CW} \sim 0.29$ K. Scaling the energy scale by a factor of 2 reproduces the experimental observation $\theta_{\rm CW} \sim 0.53$ K (ref. 24). δ and q are nearly within error bars of the analysis given in ref. 20. However, we note that if we take $|\delta|$ to be comparable to q and/or take a much larger value of $|K|$, e.g., $K = -1.2$, following ref. 20, the intensity at the scattering branch from (111) to (220) in the SF channel is significantly suppressed, in disagreement with our experiments. The nearest-neighbour coupling constants from H_D are of the order of 0.01 K, namely, one or two orders of magnitude smaller than the superexchange couplings of our choice, though they give rise to ~ -0.2 K in the energy eigenvalue of the mean-field Hamiltonian. This might cause other minor differences. As also noted in ref. 20, the parameters δ, q, and K we have obtained are quite different from the estimates by Thompson *et al.*[44] who analysed the Hamiltonian including all the crystal field states but only the same number of coupling constants without any multipolar interactions.

In Supplementary Figs. S4 a and b, we show the temperature dependence of the calculated neutron-scattering intensity in the SF channel (without taking account of the form factor) along the $[11-1]$ and $[111]$ cuts through the (111) point, respectively. It is clear that the intensity along the $[11-1]$ cut is not only enhanced but also sharpened with decreasing temperature down to 0.3 K, while that along the $[111]$ cut remains almost featureless even at 0.3 K. This is consistent with the picture that the high-temperature phase of this model is described as a Coulomb phase characterized by a remnant of a pinch-point singularity.

The mean-field ground state was obtained from the same scheme as employed above. We searched for the lowest-energy states among the classical energies per site,

$$E_{cl,\boldsymbol{Q},n} = \frac{\varepsilon_{\boldsymbol{Q},n}}{Max_i \sum_\mu |\phi^\mu_{\boldsymbol{Q},n,i}|^2}. \tag{S19}$$

Then, the MF ground state is found by approaching the (000) point from the $[100]$ direction, resulting in the noncoplanar pseudospin structure and the nearly collinear ferromagnetic structures shown in Figs. 1b and 1c of the main text, respectively.

Note that the possibility of an ordered spin-ice state[10,45,46] is ruled out, since it should create magnetic Bragg peaks at (100), in contradiction to our findings and cannot explain the neutron depolarisation due to the macroscopic magnetic moment.

Supplementary References

41. Gardner, J., Ehlers, G., Rosov, N., Erwin, R. W. & Pertovic, C. Spin-spin correlations in $Yb_2Ti_2O_7$: a polarized neutron scattering study. *Phys. Rev. B* **70**, 180404(R) (2004).

42. Ross, K. A., Ruff, J. P. C., Adams, C. P., Gardner, J. S., Dabkowska, H. A., Qiu, Y., Copley, J. R. D. & Gaulin, B. D. Two-dimensional kagome correlations and field induced order in the ferromagnetic XY pyrochlore $Yb_2Ti_2O_7$. *Phys. Rev. Lett.* **103**, 227202 (2009).

43. Enjalran, M. & Gingras, M. J. P. Theory of paramagnetic scattering in highly frustrated magnets with long-range dipole-dipole interactions: The case of the $Tb_2Ti_2O_7$ pyrochlore antiferromagnet. *Phys. Rev. B* **70**, 174426 (2004).

44. Thompson, J. D., McClarty, P. A., Rønnow, H. M., Regnault, L. P., Sorge, A. & Gingras, M. J. P. Rods of neutron scattering intensity in $Yb_2Ti_2O_7$: compelling evidence for significant anisotropic exchange in a magnetic pyrochlore oxide. *Phys. Rev. Lett.* **106**, 187202 (2011).

45. Siddharthan, R., Shastry, B. S. & Ramirez, A. P. Spin ordering and partial ordering in holmium titanate and related systems. *Phys. Rev. B* **63**, 184412 (2001).

46. Melko, G. R. & Gingras, M. J. P. Monte Carlo studies of the dipolar spin ice model. *J. Phys. Condens. Matter* **16**, R1277-R1319 (2004).